Effects on the resolution of the near-wake by the use of different meshes using RANS and URANS

Aa Madsen, M. H.; Zahle, F.; Sørensen, N. N.; Bottasso, C. L.

Published in:
The Science of Making Torque from Wind (TORQUE 2024): Modeling and simulation technology

Link to article, DOI:
10.1088/1742-6596/2767/5/052047

Publication date:
2024

Document Version
Publisher's PDF, also known as Version of record

Effects on the resolution of the near-wake by the use of different meshes using RANS and URANS

Effects on the resolution of the near-wake by the use of different meshes using RANS and URANS

M H Aa Madsen[1,2], F Zahle[2], N N Sørensen[2], C L Bottasso[1]

[1]Wind Energy Institute, Technische Universität München, D-85748 Garching b. München, Germany

[2]Technical University of Denmark, Department of Wind and Energy Systems, Frederiksborgvej 399, 4000 Roskilde, Denmark

E-mail: mads.madsen@tum.de

Abstract. This work compares the wake resolution for several meshes in order to find an accurate yet computationally efficient grid. The mesh is identified through a parametric study where the wake resolution is gradually increased using up to 55 million cells. The mesh is designed in order to support CFD-based shape design, considering not only the wind turbine power but also an improved wake recovery. Furthermore, a comparison between steady-state and transient RANS formulations is presented. The proposed meshing should allow for extending a recently published CFD-based shape design focusing on wind turbine power, to also include wake behavior in an optimization context.

1 Introduction

The flow immediately behind a wind turbine rotor, known as the wake, is a region of highly complex phenomena and it has –as a consequence– been studied in great detail both experimentally [1, 2] and numerically [3, 4]. As knowledge of the underlying phenomena at play increases, a logical next step is then to attempt to control the wake to, e.g., promote a faster wake recovery [4].

Comparative studies [5] show that numerical investigations can indeed capture overall trends of experimental investigations into wake manipulation. Blade shape changes have also been investigated [1, 4] as a way to promote a faster wake recovery, either by extending a single blade [4] (which –breaking the symmetry– induces a premature leap-frogging), or by general shape changes [1].

This work contains preparatory studies to support future CFD-based shape design that aim at combining rotor performance with an accelerated wake recovery. The starting point for this work was the mesh used in a recent design study [6], where the IEA 10 MW reference wind turbine [7] was optimized by adding a novel tip shape, resulting in an increased power at similar loads. In order to extend the capabilities of that study to also optimize for (near-)wake entrainment, a new mesh topology with improved resolution in the wake region is tested here. Using a parametric study, an accurate yet cost-efficient CFD mesh is identified. The present study also offers a comparison between steady-state and transient RANS. As the former is much cheaper and will be used for the design optimizations, this comparison serves to quantify possible limitations due to the use of the steady model instead of the unsteady one.

The remaining sections are organized as follows. Section 2 presents the numerical setup and overall methodology whereafter an initial analysis of the meshes is given in Sec. 3. The results are then presented in Sec. 4. Finally, conclusions are summarized in Sec. 5.

2 Methodology

All meshes and simulations have been carried out with in-house tools: surface meshes were prepared with the Parametric Geometry Library (PGL) [8], after which the volume meshes were obtained with the hyperbolic mesh generator HypGrid [9] and PGL.

2.1 Meshing

The surface mesh was modelled with 256 cells in the chordwise direction and 128 cells in the spanwise direction. Using a block size of 32×32 and adding four extra blocks to form the tip cap for each blade, a total of 108 surface mesh blocks were used, amounting to 110592 cells. The surface mesh for this study described above is exactly the same as the surface mesh in a recent design study [6].

However, the volume mesh used in the previous study is spherical, resulting in poor cell distribution in the wake. Therefore, it is necessary to introduce a new volume mesh, which is capable of more accurately resolving the flow field in the wake region. To this end, a bullet-like mesh topology is chosen to replace the spherical rotor mesh. A comparison of the two meshes can be seen in Fig. 1. The two meshes are further compared in Sec. 3.

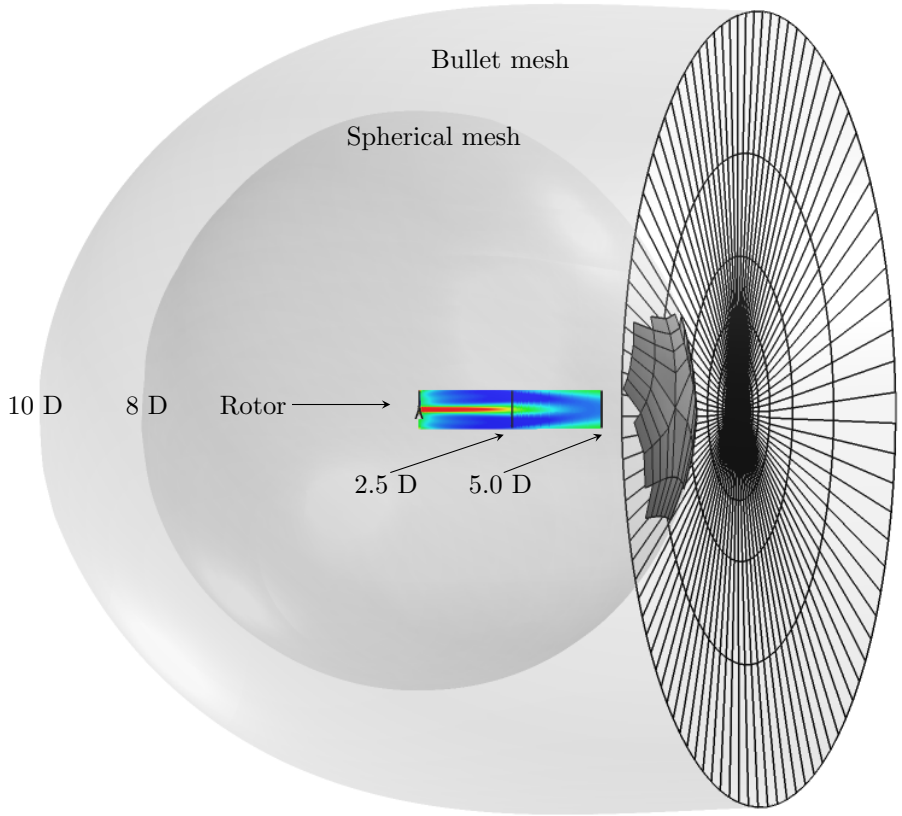

Figure 1: Comparison of spherical and bullet meshes with inflow zone (transparent gray) and outflow zone (black grid lines). The two meshes have the same type of boundary conditions. The flow field inset covers 0 D to 5.0 D, which is the wake region of interest in this study.

2.2 CFD simulations and operational conditions

The incompressible pressure-correction-based CFD flow solver EllipSys3D [10, 11, 12] is used for the flow analysis in the present study. EllipSys3D has been validated against experimental data over the last two decades [13, 14, 15] and will be used to compute steady-state and unsteady RANS solutions. The third-order accurate QUICK scheme will be used in all simulations for the convective terms. The operational conditions are identical to the ones used in ref. [6], and can be inspected in Tab. 1. It should be noted that the solution converged slightly faster on the spherical mesh and, additionally, the

flow solver was able to use one more coarse grid solver level. The flow, being fully turbulent, is modeled without transition using the $k-\omega$ shear-stress transport (SST) turbulence model [16].

Table 1: Operational conditions: density is set to the one of air at sea level and 15 °C, $\rho = 1.225$ $[kg\ m^{-3}]$, dynamic viscosity is set to $\mu = 1.784 \cdot 10^{-5}$ $[kg\ m^{-1}\ s^{-1}]$.

Wind speed $[m/s]$	**RPM** $[-]$	**Pitch** $[deg]$	**TSR** $[-]$
8.0	8.164590	0.0	10.58

3 CFD mesh comparison

In this section, the two mesh topologies are compared using RANS flow fields computed with the operational conditions from Tab. 1. The rotor geometry has a slight modification compared to the IEA 10 MW reference wind turbine, which allows the flow solver to reach machine accuracy for all the steady-state cases presented in this work. It should be noted that the mesh modification only changes the spanwise forces towards the blade root, while forces on the outer part of the blade are unaltered [6, Fig. 5].

From the overview given in Fig. 1, comparing the spherical mesh and the bullet mesh, it is clear that the latter has a much higher cell concentration in the wake region, which is particularly evident when inspecting the outflow zone. This is achieved despite only using 15 % more cells.

Another difference is that the bullet mesh covers a slightly larger domain in all directions, reaching 10 D upstream instead of the 8 D of the spherical mesh. Choosing the bullet mesh over the spherical one offers the benefit that it is now possible to easily increase cells in the cylindrical wake zone if necessary. This will be further analysed in Sec. 4.

The overall mesh quality is determined by many factors, e.g., orthogonality, cell aspect ratio, and stretching. The streamwise cell stretching of the bullet mesh, which in this study is called MeshA, can be inspected in Fig. 2, while the radial cell stretching is shown in Fig. 1.

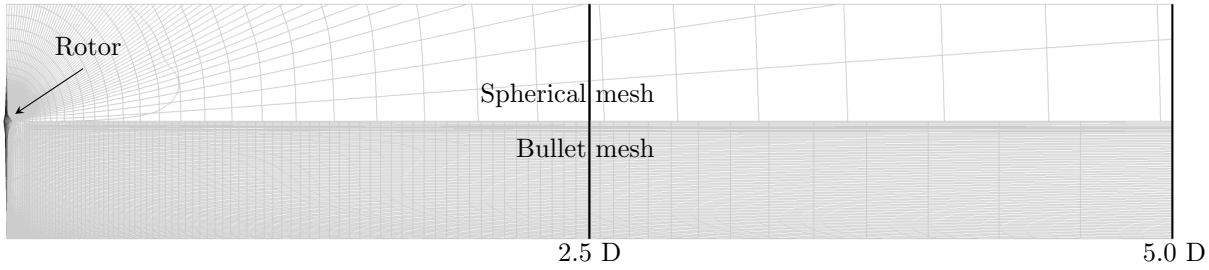

Figure 2: Comparison of spherical mesh (upper half) and bullet mesh (lower half), showing that the latter has a much higher cell density in the wake region despite only using 15 % more cells.

It is evident from Fig. 2 that there are two overall regions: a near-wake region (in the range $0-2.5$ D) with a high cell density, and a region with much higher streamwise cell stretching between 2.5 D and 5.0 D. The cell distribution has been selected in this way to capture as much as possible of the influence of the rotor geometry on the flow in the near-wake region.

3.1 Mesh convergence

To examine the mesh dependence of the flow field for both mesh types, a mesh convergence study is carried out for the three finest grid levels (L1, L2, and L3) of each mesh. Starting from the finest grid level, termed L1, a coarsened grid level, termed L2, is generated by removing every second grid line. Repeating the coarsening procedure produces grid level L3. Richardson extrapolations are used to compute an estimate of the solution 'error'. To this end, an estimate of the 'true' value (also known as the continuum value, f_c) is needed. This is obtained as [17, eq. 3]:

$$f_c \approx f_1 + \frac{f_1 - f_2}{r^2 - 1}, \tag{1}$$

where f_1 is the value on mesh level L1, f_2 is the value on mesh level L2, and $r = 2$. The integrated metrics torque and thrust are used for the gauge function f. Table 2 and 3 show the resulting mesh convergence study for the spherical rotor mesh and the bullet one, respectively.

Spherical mesh	**Cells** [million]	**Torque** $\cdot 10^6$[Nm]	**Error** [%]	**Thrust** $\cdot 10^6$[N]	**Error** [%]
L3	0.221	5.676	10.5	1.169	6.2
L2	1.769	5.394	5.0	1.124	2.1
L1	14.155	5.200	1.3	1.106	0.5
Extrapol.	∞	5.136	0.0	1.101	0.0

Table 2: Mesh convergence results for a grid sequence from the spherical rotor mesh. This table is reproduced from [6, Tab. 3].

Bullet mesh	**Cells** [million]	**Torque** $\cdot 10^6$[Nm]	**Error** [%]	**Thrust** $\cdot 10^6$[N]	**Error** [%]
MeshA: L3	0.255	3.719	28.2	1.061	3.2
MeshA: L2	2.040	4.940	4.7	1.087	0.8
MeshA: L1	16.318	5.120	1.2	1.094	0.2
Extrapol.	∞	5.181	0.0	1.096	0.0

Table 3: Mesh convergence results for a grid sequence from the bullet mesh called MeshA.

Inspecting Tab. 2 and 3 it is reassuring that the torque and thrust values on the finest mesh level agree within 1.6 % and 1.1 %, respectively. This is achieved with very different volume mesh topologies, as only the surface mesh is identical. Also the error percentages in Tab. 2 and 3 look comparable. An error improvement factor of ~ 4 can be seen for all the L2→L1 grid changes and one L3→L2 grid level change. However, the remaining L3→L2 grid level changes have differing error improvement factors. This indicates that the L3 solutions are outside the asymptotic range and should only be used to speed up computations.

The mesh convergence study, including the Richardson extrapolations, are visualized in Fig. 3. As seen, the extrapolated values almost coincide and only differ by 0.9 % and 0.4 % for torque and thrust, respectively. Once again, this underlines the overall agreement between the two meshes, despite having very different volume mesh topologies.

To translate these mesh convergence results into more generally applicable meshing recommendations for CFD-based blade design, it would be necessary to include evaluations with other differencing schemes and flow solvers.

3.2 RANS flow field comparison

Figure 4 shows the RANS flow fields for both meshes. Comparing the streamwise flow fields, it is evident that the flow is much better resolved due to the increased cell concentration between $0 - 5\ D$, which is the region of interest for this study. Furthermore, the tip vortices are resolved farther downstream, as can be expected for a higher mesh resolution.

4 Results

The results fall in two parts. First, a parametric study in Sec. 4.1 investigates the benefit of increasing cell density in the wake region. Secondly, a comparative study in Sec. 4.2 investigates discrepancies between steady-state and unsteady RANS computations.

4.1 Near-wake resolution

In this parametric study, the cell density in the near-wake region ($0 - 2.5\ D$) will be gradually increased to test four different resolutions. Figure 5 shows visualizations of the resulting flow field as the cell concentration in the wake region is increased from $5 \cdot 10^6$ to $44 \cdot 10^6$.

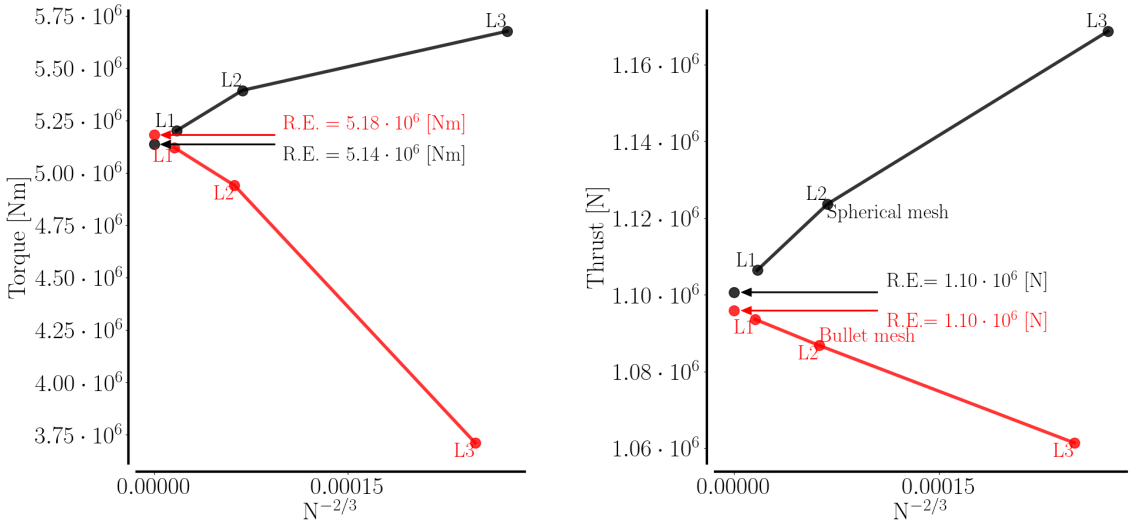

Figure 3: Richardson extrapolations for the spherical mesh and for the bullet mesh. Further details are listed in Tab. 2 and 3.

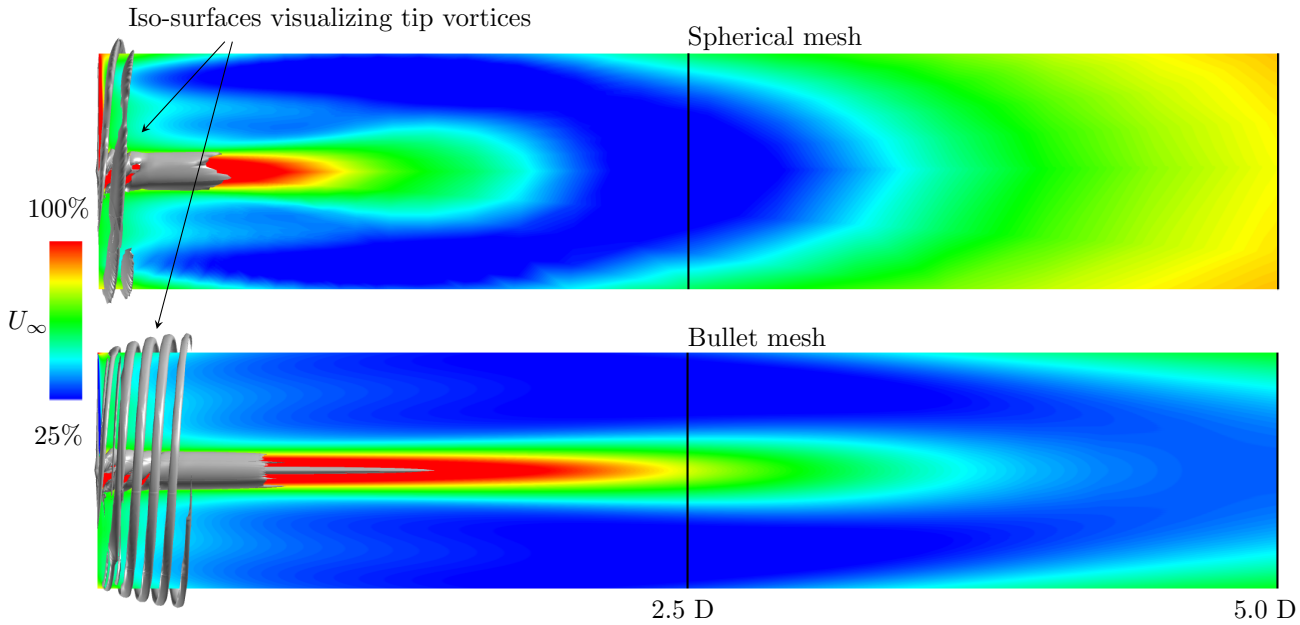

Figure 4: Streamwise velocity fields. The bullet mesh captures the flow field and tip vortices much better despite only using 15 % more cells. Tip vortices are visualized using the Q-criterion of the velocity field; the threshold is fixed to the same value for all visualizations in the remaining figures.

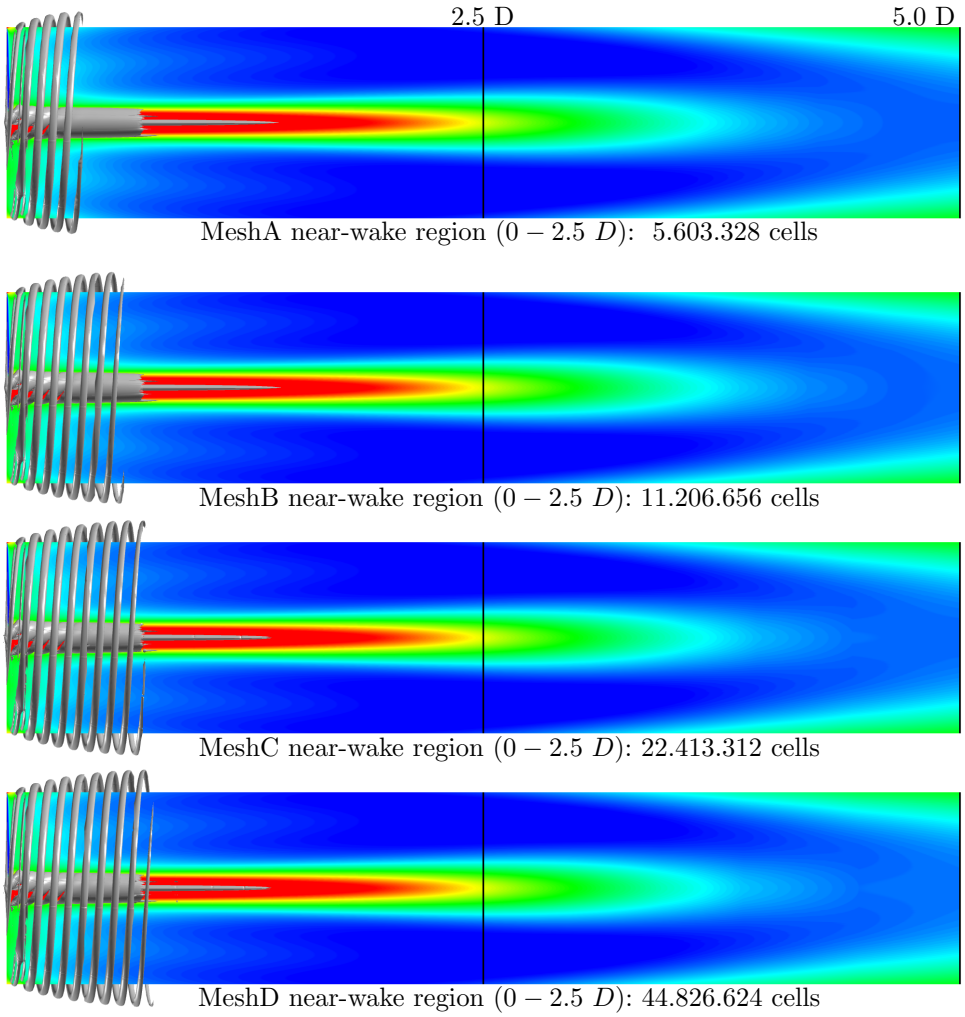

Figure 5: Parametric study of the cell resolution in the wake region, showing a noticeable improvement of tip vortex resolution between the two coarsest meshes. The two finest meshes, on the other hand, have comparable tip vortex resolutions. The main characteristics of all meshes are given in Tab. 4.

As seen in the figure, the tip vortex resolution increases significantly by doubling the cell count once (MeshA compared to MeshB). On the other hand, there is not much to be gained from further doubling the amount of cells in the near-wake region $0 - 2.5\ D$. With respect to the visualized flow fields, there is no discernible difference to warrant an increase in cell concentration. Comparing the streamwise velocity wake deficits at 2.5 D for MeshA and MeshB, it appears the error changes only by 0.3 %, underlining that even the two coarsest meshes have comparable performance. To avoid redundancy, wake deficit comparison plots have been omitted since no discernible difference can be seen.

The parametric study for cell concentration in the near-wake region is summarized in Tab. 4. The errors have been computed with Richardson extrapolation using Eq. (1), and the full grid sequence convergence studies can be found in appendix A. Furthermore, the grid sequences are also visible in Fig. 6.

Mesh	Mesh cells [million]	Near-wake cells [million]	Torque $\cdot 10^6$[Nm]	Error [%]	Thrust $\cdot 10^6$[N]	Error [%]
Bullet mesh: MeshA	16.318	5.603	5.120	1.2	1.094	0.2
Bullet mesh: MeshB	21.922	11.207	5.119	1.2	1.094	0.2
Bullet mesh: MeshC	33.128	22.413	5.120	1.2	1.094	0.2
Bullet mesh: MeshD	55.542	44.827	5.120	1.2	1.094	0.2

Table 4: Mesh convergence results showing low error percentage for both torque and thrust compared to extrapolated Richardson values for each mesh. The full mesh convergence study can be found in appendix A. The near-wake region is set to $0 - 2.5\ D$.

As expected, Tab. 4 shows that the low error percentage on torque and thrust obtained for MeshA is unchanged for the finer meshes, given that it is only the cell resolution in the wake region that changes. To further improve torque and thrust, it would be necessary to refine the underlying surface mesh, which for this study is kept fixed.

The positive outcome of the convergence study in Tab. 4 is that there is no need to select a mesh with a finer wake resolution than MeshA, when considering CFD-based shape optimizations focusing on torque or thrust. This is reassuring, given that MeshA has $16 \cdot 10^6$ cells, which is close to the maximum of what one could expect to include in a CFD-based design at present. However, since an increase in tip vortex resolution is observed in Fig. 5 between MeshA and MeshB, it is MeshB that is finally chosen for performing a comparison to transient CFD models in Sec. 4.2.

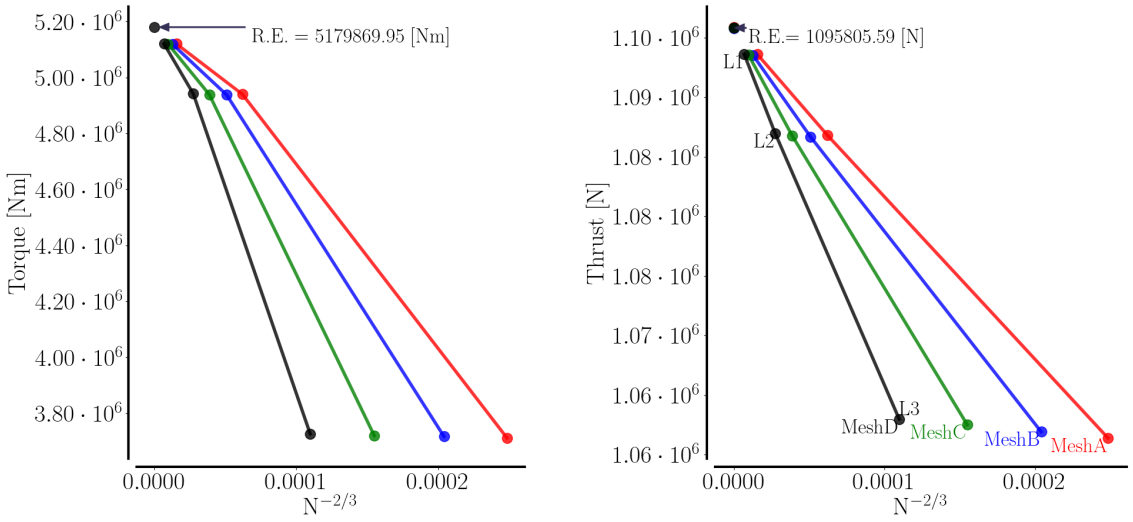

Figure 6: Richardson extrapolations for the meshes seen in Tab. 4. Further details can be found in Tab. 3 in Sec. 3 and tables 5, 6, and 7 in appendix A.

4.2 Comparison between steady-state and transient RANS flow models

Having identified MeshB from Tab. 4 as the most cost efficient yet accurate bullet mesh, it will now be used to compare steady-state and unsteady RANS flow fields.

For correct transient computations, it is important to select a small enough time step. A time step of $dt = 5 \cdot 10^{-3}$ $[s]$ was set, matching the rule-of-thumb that the rotor should not rotate more than 1/4 degree per time step. Comparing the torque to a simulation with $dt = 1 \cdot 10^{-2}$ $[s]$ showed a difference of less than 0.2 %, signifying that the time step is indeed small enough. To ensure that the URANS computation is fully converged, the simulation time is set to 8 times the flow-through time in the streamwise direction for the bullet mesh. There are 2 times domain flow-through on both the L3 and L2 meshes, and 4 times domain flow-through for the L1 mesh. The time stepping is based on a second order scheme, and up to 8 subiterations are taken within each time step to reach convergence.

The inflow is steady and the rotor axis is aligned with the flow. Although the rotor is highly loaded and locally exceeds the Betz limit at $C_T = 8/9$, for the chosen operational conditions the flow is expected to be quite steady, except for any turbulence developing around and behind the rotor. Therefore, an overall agreement between RANS and URANS should be expected, once the initial transient has disappeared in the latter.

A comparison of the flow fields is shown in Fig. 7. The RANS and URANS solutions do indeed closely match each other. The URANS flow field is not averaged, and the figure represents an instantaneous snapshot after reaching convergence on L1. The only visible difference is the upwards-pointing blade in the RANS case, which is not visible in the URANS visualization due to the fact that the simulation was stopped at a time step that did not correspond to a full rotor revolution (the URANS rotor blade is pointing directly against the direction of view, making it hard to discern).

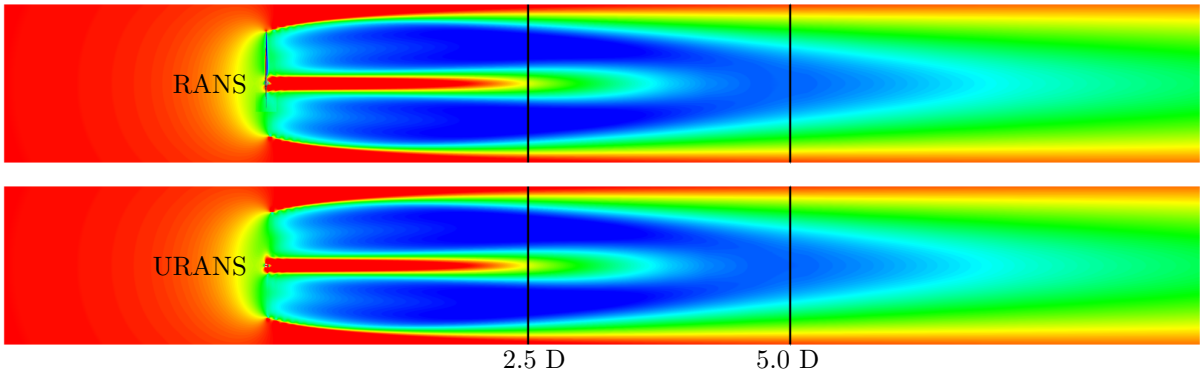

Figure 7: Streamwise velocity comparison of RANS (top) and URANS (bottom). Comparisons of the wake deficits at 2.5 D and of 5.0 D can be further inspected in Fig. 8.

The comparison of instantaneous wake deficits may occasionally show sign of a tip vortex, when a wake deficit is probed through one of them. This was avoided by performing an azimuthal averaging of the solution. The averaged results for RANS and URANS can be seen in Fig. 8 and, as it is evident from a comparison between the two, they match very well. In fact, the RANS and URANS wake deficits do not differ more than 0.4% and 0.2% at 2.5 D and 5.0 D, respectively.

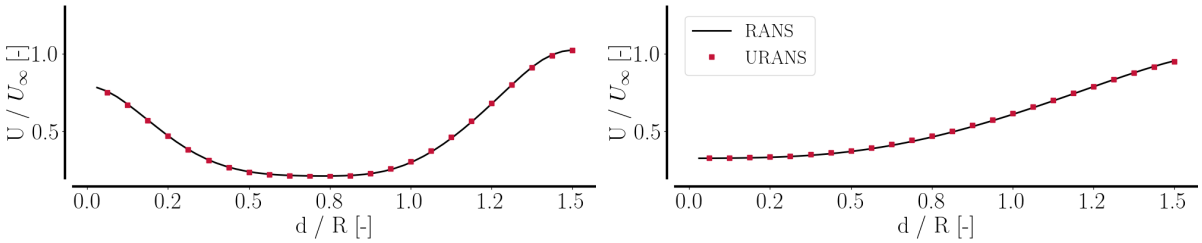

Figure 8: Azimuth-averaged wake deficit comparison, indicating maximum errors of 0.4% (2.5 D, left) and 0.2% (5.0 D, right). The flow fields in the wake region can be inspected in Fig. 7.

5 Conclusion

A suitable mesh to be used in CFD-based shape design has been identified through a parametric study. The comparative results show that the so-called bullet mesh allows for a much better resolved wake region. The load predictions on the bullet mesh reassuringly agree with the ones obtained on the so-called spherical mesh to within 1.6 % for torque and 1.1 % for thrust, respectively.

Furthermore, a comparison between steady-state and transient flows has shown that, for the chosen operating conditions, there is a close match between RANS and URANS simulations. This indicates that optimizations can be performed with the less expensive RANS without loss of accuracy.

Acknowledgements

This project has received funding from the European Union's Horizon 2020 research and innovation programme under the Marie Skłodowska-Curie grant agreement No 899987. The authors gratefully acknowledge the computational and data resources provided on the Sophia HPC Cluster at the Technical University of Denmark [18].

A Appendix

This appendix contains the full convergence results for each mesh used in the study of Sec. 4.

Four bullet meshes (MeshA, MeshB, MeshC, and MeshD), with increasing cell resolution in the near-wake region ($0 - 2.5\ D$), have been tested in a grid convergence study covering the three finest grid levels (L1, L2, and L3). The convergence for MeshA can be found in Tab. 3. The convergence for MeshB, MeshC, and MeshD can be found in Tab. 5, 6, and 7. There is a persistent high torque error on L3 as the mesh is refined. This is due to the fact that torque is not significantly dependent on the wake resolution, whereas it does strongly dependent on the surface mesh. Given that the surface mesh remained the same for all meshes, it is to be expected that the torque error is largely unaltered.

Bullet mesh	**Cells** [million]	**Torque** $\cdot 10^6$[Nm]	**Error** [%]	**Thrust** $\cdot 10^6$[N]	**Error** [%]
MeshB: L3	0.343	3.726	28.1	1.062	3.1
MeshB: L2	2.740	4.938	4.7	1.087	0.8
MeshB: L1	21.922	5.119	1.2	1.094	0.2
Extrapol.	∞	5.180	0.0	1.096	0.0

Table 5: Mesh convergence results for a refinement sequence of MeshB.

Bullet mesh	**Cells** [million]	**Torque** $\cdot 10^6$[Nm]	**Error** [%]	**Thrust** $\cdot 10^6$[N]	**Error** [%]
MeshC: L3	0.518	3.732	28.0	1.063	3.0
MeshC: L2	4.141	4.939	4.7	1.087	0.8
MeshC: L1	33.128	5.120	1.2	1.094	0.2
Extrapol.	∞	5.180	0.0	1.096	0.0

Table 6: Mesh convergence results for a refinement sequence of MeshC.

Bullet mesh	**Cells** [million]	**Torque** $\cdot 10^6$[Nm]	**Error** [%]	**Thrust** $\cdot 10^6$[N]	**Error** [%]
MeshD: L3	0.868	3.719	27.8	1.063	3.0
MeshD: L2	6.943	4.942	4.6	1.087	0.8
MeshD: L1	55.542	5.120	1.2	1.094	0.2
Extrapol.	∞	5.180	0.0	1.096	0.0

Table 7: Mesh convergence results for a refinement sequence of MeshD.

References

[1] Abraham A and Leweke T 2023 *Experiments in Fluids* **64**(6) 12

[2] Campagnolo F, Castellani F, Natili F, Astolfi D and Mühle F 2022 *Frontiers in Energy Research* **10** ISSN 2296-598X URL `https://www.frontiersin.org/articles/10.3389/fenrg.2022.883889`

[3] Sørensen J N, Mikkelsen R F, Henningson D S, Ivanell S, Sarmast S and Andersen S J 2015 *Phil. Trans. of the Royal Society A* **373** 20140071

[4] Abraham A, Ramos-Garcia N, Sørensen J N and Leweke T 2023 *Journal of Physics: Conference Series* **2505** 012032 URL `https://dx.doi.org/10.1088/1742-6596/2505/1/012032`

[5] Wang J, Wang C, Campagnolo F and Bottasso C L 2019 *Wind Energy Science* **4** 71–88 URL `https://wes.copernicus.org/articles/4/71/2019/`

[6] Madsen M H A, Zahle F, Horcas S G, Barlas T K and Sørensen N N 2022 *Wind Energy Science* **7** 1471–1501

[7] Bortolotti P, Tarrés H C, Dykes K, Merz K, Sethuraman L, Verelst D and Zahle F 2019 IEA wind TCP task 37: Systems engineering in wind energy-wp2.1 reference wind turbines Tech. rep.

[8] Zahle F 2020 PGL: parametric geometry library URL `https://gitlab.windenergy.dtu.dk/frza/PGL`

[9] Sørensen N 1998 HypGrid2D a 2-D mesh generator Tech. rep. Risø National Laboratory

[10] Michelsen J 1992 Basis3D - a platform for development of multiblock PDE solvers Tech. Rep. AFM 92-05 Department of Fluid Mechanics, Technical University of Denmark

[11] Michelsen J A 1994 Block structured multigrid solution of 2D and 3D elliptic PDE's Tech. Rep. AFM 94-06 Department of Fluid Mechanics, Technical University of Denmark

[12] Sørensen N 1995 *General purpose flow solver applied to flow over hills* Ph.D. thesis Risø National Laboratory Frederiksborgvej 399, 4000 Roskilde

[13] Sørensen N, Michelsen J and Schreck S 2002 *2002 Asme Wind Energy Symposium; 40. AIAA Aerospace Sciences Meeting and Exhibit* 94–105

[14] Bechmann A, Sørensen N and Zahle F 2011 *Wind Energy* **14** 677–689 ISSN 10991824, 10954244

[15] Grinderslev C, González Horcas S and Sørensen N N 2021 *Wind Energy* **24** 1426–1442

[16] Menter F 1993 *24th Fluid dynamics conference* AIAA 1993–2906 URL `https://arc.aiaa.org/doi/abs/10.2514/6.1993-2906`

[17] Roache P J 1994 *Journal of Fluids Engineering* **116** 405–413 ISSN 0098-2202

[18] Technical University of Denmark 2019 Sophia HPC cluster URL `https://dtu-sophia.github.io/docs/`